Physica B 666 (2023) 415107

Contents lists available at ScienceDirect

Physica B: Condensed Matter

journal homepage: www.elsevier.com/locate/physb

Mean-Field and Monte Carlo calculations of phase transitions in a core–shell Ising nanotube

M. Karimou [a,b], T.D. Oke [b], S.I.V. Hontinfinde [c], J. Kple [b,d], F. Hontinfinde [b,d,*]

[a] Ecole Nationale Supérieure de Génie Energétique et Procédés (ENSGEP), Université d'Abomey, Benin
[b] Institut de Mathématique et de Sciences Physiques, Université d'Abomey-Calavi, Benin
[c] Ecole Nationale Supérieure de Génie Mathématique et Modélisation (ENSGMM), Université d'Abomey, Benin
[d] Faculté des Sciences et Techniques, Université d'Abomey-Calavi, Benin

ARTICLE INFO

Keywords:
Ising nanotube
Mean-field theory
Monte Carlo method
Magnetic field
Phase transitions
Magnetic hysteresis

ABSTRACT

A cylindrical Ising nanotube that consists of 3/2 core spins surrounded by 5/2 shell spins is introduced and studied with Mean-Field approximation and Monte Carlo simulations in the presence of crystal and external magnetic fields. The effects of positive and negative interfacial coupling constants on the magnetic properties have been examined. The thermal behaviors of the order parameters and different types of macroscopic instabilities are presented. The model exhibits compensation points, first- and second-order phase transitions. Richer magnetic properties are obtained in the antiferromagnetic core–shell coupling case. In the presence of ferromagnetic interfacial coupling, the simulations sometimes generated long-lived metastable states. These states jumped to stable thermodynamic ones under thermal fluctuations via first-order phase transitions.

1. Introduction

An intense research focused on nanostructured materials [1,2] (nanoparticles, nanorod, nanowire, nanotube) in recent years because of their potential applications in several technological domains: biomedicine [3–5], magnetic resonance imaging [6], permanent magnets [7], magnetic storage and recording media [8–11], plastics and carbon fibers strengthening [12], building structural materials reinforcing [13], sensors [14], catalysts, energy conversion and storage, etc. Their physical properties are related to their size and dimensionality and this motivated much theoretical investigations and unexpected properties have been discovered. A current challenging problem in the field is how to develop using materials of different nature, efficient and low-cost multifunctional nanoparticles. Compounds as Zn–ZnO, Fe–Pt, Fe_3O_4 [15,16] nanotubes are typical examples that received an important focus of attention. They can be manufactured in several geometric forms: cubic, hexagonal, cylindrical, etc. It has been shown that cylindrical core/shell nanotubes are very performant. The shell material can play the role of protector against oxidation and corrosion in an hostile environment [17]. Carbon-made shell nanoparticles are more interesting for several reasons. They can generate nanoparticles that are compatible with biological systems [3]. Moreover, they present physical features that can make them good candidates to replace silicon in future advanced electronic devices. Experimentally, nanotubes have been manufactured by means of various techniques including chemical vapor deposition (CVD) process, Laser vaporization, hydrothermal reaction, electro-deposition method, etc. Mathematical models of nanotubes comprise Ising models where spins of the core are surrounded by spins of the shell. It is worthwhile to mention that Ising systems are the most studied many-body systems because they can describe quite well most physical systems as lattice spin systems, binary alloys, etc [18]. Ising nanotube models have been solved using number of statistical–mechanical methods including the Mean-Field (MF) theory [19], the Effective Field Theory (EFT) [18,20], numerical simulations by Monte Carlo (MC) [21,22] or Cellular Automata (CA) [23], etc. Kaneyoshi studied critical and compensation temperatures in a hexagonal spin-1/2 Ising nanotube by means of EFT with correlations [18]. Masrour et al. investigated using Monte Carlo simulations, magnetic properties of a mixed-spin (1, 3/2) core/shell hexagonal Ising nanotube [24]. They have observed interesting properties, in particular critical and triple hysteresis behaviors. Other attracting magnetic properties have been reported on Ising nanotubes in Refs. [25–28] and on nanographene in [29,30]. The CoPt nanotube was investigated in the presence of an external magnetic field in [31]. A particular interest has been devoted to the study of the magnetism of nanowires/nanotubes of other transition metals alloys as FePt, FePd, CoPd, etc due to their involvement as critical elements in many different applications and devices, in particular in digital communication [32–36].

In this paper, a mixed-spin (3/2, 5/2) core/shell nanotube with equal number of spins in the core and shell, is introduced and studied

* Corresponding author at: Institut de Mathématique et de Sciences Physiques, Université d'Abomey-Calavi, Benin.
E-mail address: fhontinfinde@yahoo.fr (F. Hontinfinde).

https://doi.org/10.1016/j.physb.2023.415107
Received 4 November 2022; Received in revised form 26 May 2023; Accepted 30 June 2023
Available online 5 July 2023

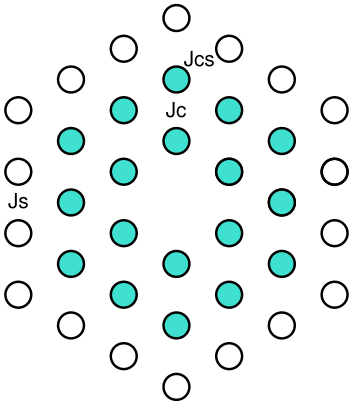

Fig. 1. Schematic representation of a nanotube with three cylindrical layers. Colored (full) circles represent core atoms with spin 3/2. Open circles are surface shell atoms with spin 5/2. J_c, J_s and J_{cs} are nearest-neighbor coupling constants for atoms in the core, in the shell and at the core–shell interface respectively.

in the presence of crystal and external magnetic fields. A nanotube with a Co-core and a Al-shell may be a typical example. The present work is then not only important from the fundamental point of view but such a system can be a promising candidate for magnetic storage devices and can also be used in microelectromechanical systems. We will generate predictions on the magnetic properties of the system by studying phase transitions, compensation points, coercivity, magnetization saturation, magnetic susceptibility, critical points, etc. The knowledge of these key features is important for technological applications. Since the direction of the interfacial coupling between interacting surfaces in physical devices depends on many factors such as microscopic contact geometries, polarization energy, energy level alignment, etc, we will consider in the study both ferromagnetic and antiferromagnetic interfacial couplings [37,38]. A closely and geometrically related nanowire system but with different core/shell spins has been recently investigated by our research group and yielded interesting properties [39]. Another system with some resemblance is the Ising core/shell borophene structure with spins (5/2,3/2) studied in Ref. [40]. There, the ground state phase diagrams were determined as well as the variations of magnetic properties due to changes in model parameters. The present core/shell model is first formulated in the MF approximation and expressions of the order parameters are derived. In the presence of driving magnetic field, the model has been examined with MC simulations with the Metropolis update algorithm [41] in order to take into account correlations of spin fluctuations in the results. Thermal behaviors of the order parameters are presented as well as the magnetic susceptibility and the internal energy. This enabled us to construct typical thermal phase diagrams for the model for selected values of the model parameters. The model exhibits critical, compensation and first-order transition temperatures that we specified.

The paper is organized as follows. In Section 2, the model is formulated with its MF solution. Section 3 gives briefly the MC simulations method. In Section 4, the numerical results and discussion are given. Section 5 is devoted to concluding remarks.

2. Mean-field calculations

A three-cylindrical layer model comprising two core layers with N_c spin 3/2 and one layer with N_s spins 5/2 is considered. Each nanotube section (Fig. 1), has the same number of core and shell atoms with a total of $N_z = 300$ sections in the z-direction where periodic boundary conditions are applied. Due to the latters, lower values of N_z might be used since criticality may mostly concern lateral size of each section where free boundary conditions are set. The total number of spins in the system is $N_t = (N_c + N_s)$. The sections stacking procedure used has been adopted in several previous works [39]. Each section spin is connected to the two nearest-neighbor spins on the above and below sections. The number of nearest neighbors may vary from one spin to the other and for the MF calculations, average values have been used (see below). The model Hamiltonian is defined as [39,42]:

$$H = -J_c \sum_{\langle ij \rangle} \sigma_i \sigma_j - J_s \sum_{\langle kl \rangle} S_k S_l - J_{cs} \sum_{\langle ik \rangle} \sigma_i S_k - D_c \sum_i (\sigma_i)^2 - D_s \sum_k (S_k)^2 - h(\sum_i \sigma_i + \sum_k S_k) \quad (1)$$

where J_c and J_s are the exchange coupling constants between two nearest-neighbor spins at the core and surface shell, respectively; J_{cs} is an exchange interaction between two nearest-neighbor spins at the surface shell and the core. The summation indices $\langle ij \rangle$, $\langle jk \rangle$ and $\langle kl \rangle$ denote a summation over all pairs of neighboring spins at the core, shell surface and interface core/shell, respectively. We consider only the case of an uniaxial anisotropy (z) axis the same for all ions. The parameter h is a uniform external magnetic field applied parallel to the anisotropy (z) axis. The field acts on all spins $S_i = S_i^z$ and $\sigma_i = \sigma_i^z$. D_c and D_s are the core and shell lattice anisotropy constants respectively. Each related term in Eq. (1) corresponds to the single ion anisotropy energy due to crystalline field. The latter plays an important role for materials consisting of spins with values larger than 1/2. Strong enough, it induces a large energy difference between the splitted levels. Thus, it is energetically more favorable to fill low level orbitals and pair them up with opposite spins before starting to fill higher energy levels. This results in no addition to the total spin and to a low spin state [43].

The approximated free energy of the system obtained from a variational principle on the Gibbs-Bogoliubov inequality [44,45], is giving by:

$$G(H) \leq G(H_0) + \langle H - H_0 \rangle, \quad (2)$$

where $G(H)$ is the free energy of the system described by the Hamiltonian given in Eq. (1). $G(H_0)$ is the average free energy of a trial Hamiltonian H_0 which depends on variational parameters, $\langle H - H_0 \rangle$ denotes a thermal average of the value $H - H_0$ over the ensemble defined by H_0.

As the conventional procedure, the trial Hamiltonian is assumed to be in the form:

$$H_0 = -\sum_i (\lambda_c \sigma_i + D_c \sigma_i^2) - \sum_m (\lambda_s S_k + D_s S_k^2), \quad (3)$$

where λ_c and λ_s are the two variational parameters related to the molecular field acting on the two different sublattices respectively.

The expression of the variational free energy g of Eq. (2) is obtained as:

$$g = -\frac{1}{\beta}\left(\ln\left[2e^{\frac{9\beta D_c}{4}}\cosh(\frac{3}{2}\beta\lambda_c) + 2e^{\frac{\beta D_c}{4}}\cosh(\frac{1}{2}\beta\lambda_c)\right]\right) - \frac{1}{\beta}\left(\ln\left[2e^{\frac{25\beta D_s}{4}}\cosh(\frac{4}{2}\beta\lambda_s) + 2e^{\frac{9\beta D_s}{4}}\cosh(\frac{3}{2}\beta\lambda_s) + 2e^{\frac{\beta D_s}{4}}\cosh(\frac{1}{2}\beta\lambda_s)\right]\right) - z_3 J_{cs} M_c M_s + \lambda_c M_c - z_1 J_c M_c^2 + \lambda_s M_s - z_2 J_s M_s^2 - hM_c - hM_s, \quad (4)$$

where M_s and M_c are the shell and the core magnetizations respectively. Now, by minimizing the free energy in Eq. (4) with respect to λ_c and λ_s, one obtains:

$$\lambda_c = z_1 J_c M_c + z_3 J_{cs} M_s + h,$$
$$\lambda_s = z_3 J_{cs} M_c + z_2 J_s M_s + h,$$

where z_1, z_2 and z_3 are respectively the average numbers of nearest-neighbors for atoms in the core, in the shell and at the core–shell interface.

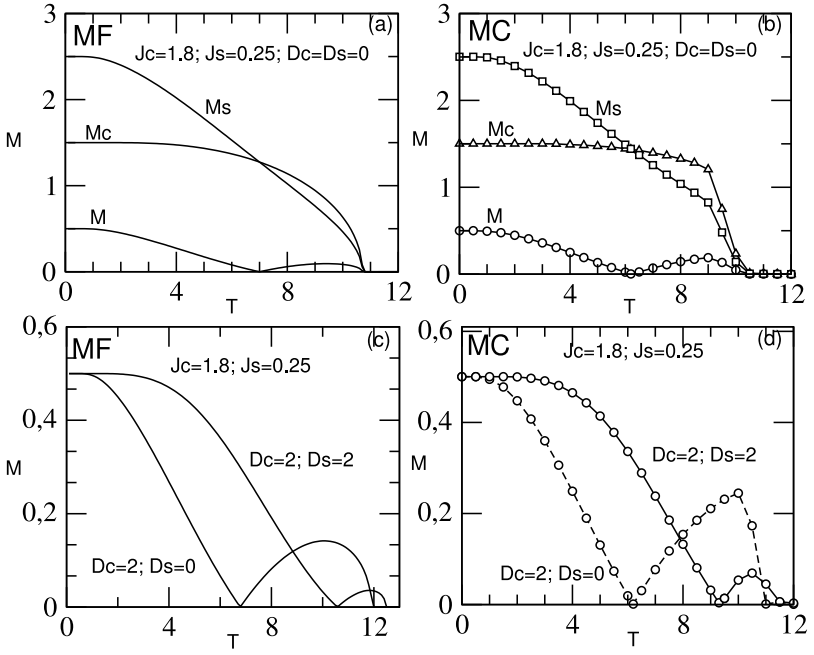

Fig. 2. Compared results on the thermal behaviors of the order parameters M_c, M_s and M by MF (panels a and c) and MC (panels b and d) for $J_{cs} = -1$ and selected values of other model parameters written in the panels. In panels c and d, the effects of core and shell crystal-fields on compensation and critical temperatures obtained in panels a and b are examined. Both calculation methods indicate that D_s has a remarkable increasing effect on the latters.

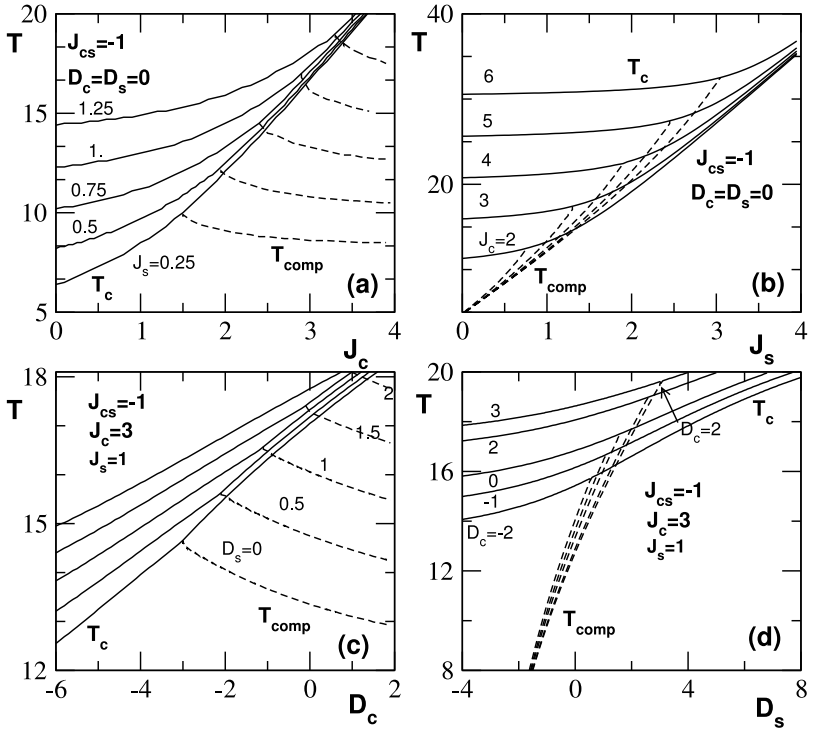

Fig. 3. Thermal phase diagrams by Mean-Field calculations for selected values of model parameters and varying coupling constants (panels a and b) and varying core and shell crystal-fields (panels c and d). Full lines are T_c-lines; dashed ones are T_{comp}-lines. The orientation of T_{comp}-lines changes when one passes from the core to the shell. In panel b, T_c-lines look parallel for small values of J_s. This also happens for T_{comp}-lines in panel c.

We determine M_c and M_s as follows:

$$M_c = \frac{3\sinh(\frac{3}{2}\beta\lambda_c) + e^{(-2\beta D_c)}\sinh(\frac{1}{2}\beta\lambda_c)}{2\cosh(\frac{3}{2}\beta\lambda_c) + 2e^{(-2\beta D_c)}\cosh(\frac{1}{2}\beta\lambda_c)}. \quad (5)$$

$$M_s = \frac{5\sinh(\frac{5}{2}\beta\lambda_s) + 3e^{(-4\beta D_s)}\sinh(\frac{3}{2}\beta\lambda_s) + e^{(-6\beta D_s)}\sinh(\frac{1}{2}\beta\lambda_s)}{2\cosh(\frac{5}{2}\beta\lambda_s) + 2e^{(-4\beta D_s)}\cosh(\frac{3}{2}\beta\lambda_s) + 2e^{(-6\beta D_s)}\cosh(\frac{1}{2}\beta\lambda_s)}. \quad (6)$$

We are interested in studying the thermal variations of the average total magnetization per site which is defined as:

$$M = \frac{M_c + M_s}{2}. \quad (7)$$

By means of this expression, one is able to determine critical temperatures while varying the Hamiltonian parameters.

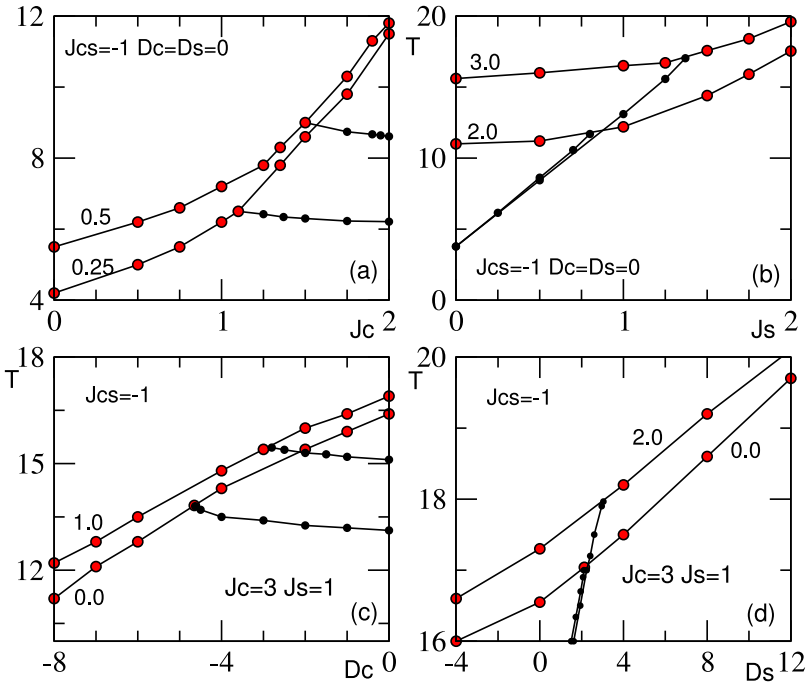

Fig. 4. Thermal phase diagrams by Monte Carlo calculations for selected values of model parameters and varying coupling constants (panels a and b) and varying core and shell crystal-fields (panels c and d). Full lines with red circles are T_c-lines; full ones with black circles are T_{comp}-lines. Compared to corresponding curves in the previous figure, T_c and T_{comp} are lower as already observed in Fig. 2 except in panel (c) where results are almost in the same order of magnitude.

3. The Monte Carlo simulation algorithm

In the Monte Carlo simulations, the Metropolis algorithm is applied [39,41,46]. A spin is randomly selected in the system. Then, one selects randomly one spin value within the possible projections with a uniform distribution probability. Another random number is chosen to decide or reject the attempted move. Physical quantities are evaluated after 10^5 to 2.10^5 MC steps per site are executed. The first 25.10^3 steps are considered for thermal equilibration and discarded in the averaging procedure. Several independent runs are often performed to get smooth data. Denoting by N_c, N_s, N_t, numbers of core, shell and nanotube spins respectively, average values of the magnetizations are calculated as follows:

$$M_c = \frac{1}{N_c}\sum_i \sigma_i; \tag{8}$$

$$M_s = \frac{1}{N_S}\sum_k S_k \tag{9}$$

and the average total nanotube magnetization

$$M = \frac{1}{N_t}(N_c \times M_c + N_s \times M_s). \tag{10}$$

At the critical temperature T_c of the system, $M(T_c) = M_c(T_c) = M_s(T_c) = 0$. The nanotube magnetic susceptibility has the expression:

$$\chi = \frac{1}{k_B T}(\langle M_t^2\rangle - \langle M_t\rangle^2) \tag{11}$$

where k_B is the Boltzmann constant, and $\langle . \rangle$ denotes a statistical average over the number of MC steps needed to reach the steady state, starting from thermal equilibrium. A peak in the behavior of χ indicates in the following, a macroscopic instability in the system.

4. Results and discussion

In the calculations, coupling constants, crystal and magnetic fields and the temperature are expressed in the same unit of energy that we denote by J_0 in the following.

4.1. Phase transitions in zero magnetic field

In this section, only an antiferromagnetic coupling constant $J_{cs} = -1$ is considered. The behaviors of the magnetizations of the system and sublattices which are the system order parameters are illustrated in Fig. 2a, c for selected values of the model parameters using the MF approximation. Results by MC calculations are illustrated in Fig. 2b, d in order to show the degree of accuracy of the MF results. First, a qualitative agreement is achieved since curves show similar trends. A certain quantitative agreement also prevails as Fig. 2a, b are concerned. We got the transition temperatures $T_c = 10.85$ by MF and $Tc = 10.05$ by MC calculations. These results are close to each other, the MF one being slightly larger than the one by MC. A similar accuracy is got from Fig. 2c, d where the effects of the crystal-field are shown. It turns out that coupling constants and anisotropies as well as thermal fluctuations have strong influences on the order parameters. One should notice two key features. First, the total magnetization vanishes before the critical temperature at the so-called compensation temperature, hereafter termed T_{comp}. Second, the change of the value of the shell crystal-field has more effect on the T_{comp} than on T_c where all order parameters vanish (see panels c and d). By comparing the total magnetizations M displayed in Fig. 2a, c, it emerges that for $D_s = 0$, changes of T_{comp} and T_c due to a non zero value of D_c are marginal. One observes that when D_c and D_s increase, T_{comp} and T_c also increase. The behavior of the system magnetic susceptibility as a function of the temperature for fixed values of other parameters has been examined. The temperature associated to its maximum is taken in the MF and MC calculations as T_c. On this basis, some thermal phase diagrams have been determined for varying values of several model parameters. The results are displayed in Figs. 3 and 4. In Fig. 3, full lines are associated to T_c whereas dashed ones are T_{comp}-lines. Let us remark that T_c-lines tend to coincide with increasing values of J_c, J_s, D_c and D_s. It emerges that values of T_c increase when coupling constant and crystal-field strength increase. The orientation of T_{comp}-lines changes as far as core and shell are concerned. The coincidence tendency is more pronounced for T_{comp}-lines for the shell material in panels b and d. Similar results have been reported in several previous works [39,46] where magnetic systems

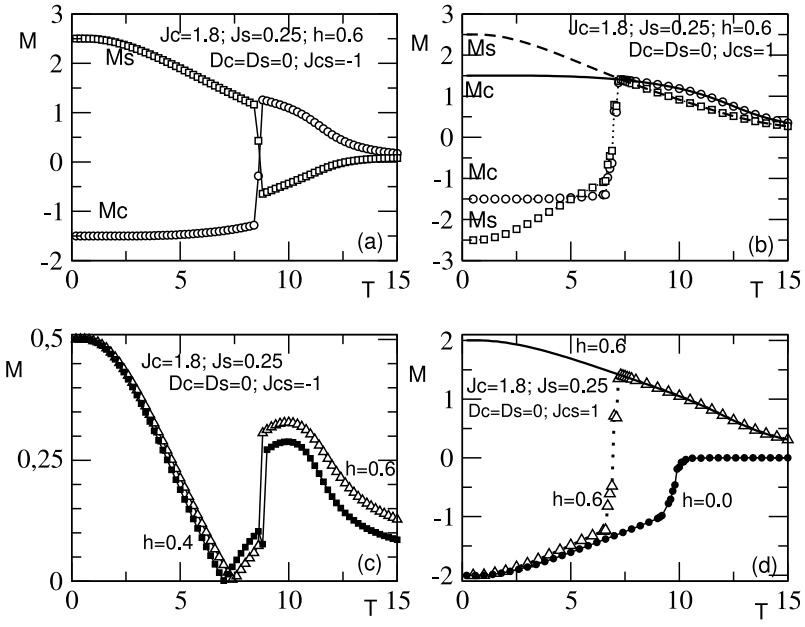

Fig. 5. Monte Carlo simulation results on behaviors of sublattice (panels a and b) and global (panels c and d) magnetizations versus temperature for some selected values of the magnetic field energy ($h = 0.4; 0.6$) starting simulations (panels a and c) from the initial configuration $(-3/2, +5/2)$. In panels b and d, two initial configurations are used: the ground-state configuration $(+3/2, +5/2)$ (full and dashed lines) and $(-3/2, +5/2)$ (symbols). Values of other model parameters are written in the panels. In panel c, compensation points are visible after which jumps appear in the magnetization curves. These jumps are associated to first-order phase transitions. In panels b and d, jumps observed correspond to a metastable-stable state transition (see text).

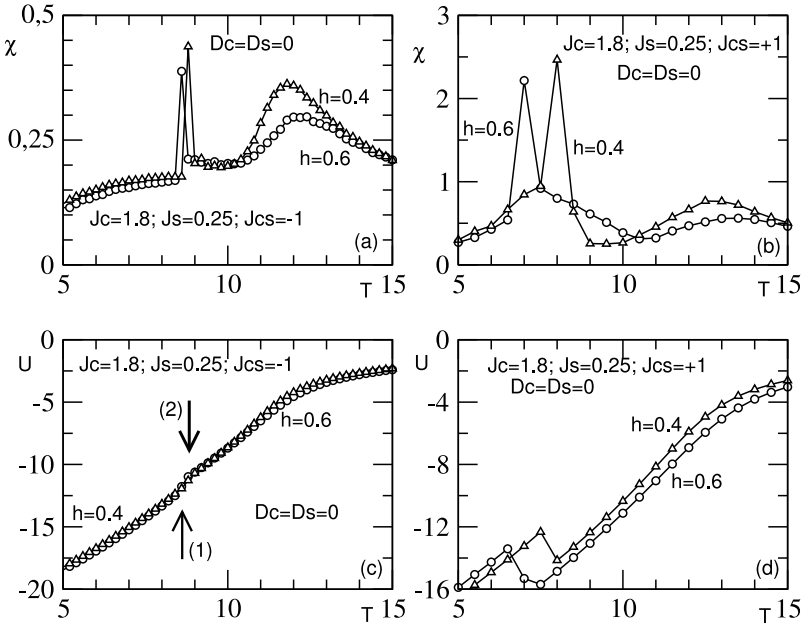

Fig. 6. Monte Carlo simulation results on the behaviors of the global magnetic susceptibility χ (panels a and b) and internal energy U (panels c and d) versus temperature for two values of the magnetic field energy and selected values of other model parameters written in the panels. Data illustrated are associated to the global magnetization M curves displayed in panels c and d of Fig. 5 for $h = 0.4$ and $h = 0.6$. Discontinuities appear in the behavior of the internal energy U. Each χ-curve shows two maxima. The height of the sharp one has been scaled in order to show the second maximum which appears broader than the first one. The first peak is associated to a first-order transition and arrows (1) and (2) (panel c) indicate such transitions in the AFM case (see text).

with inequivalent sublattices have been described by mixed-spin Ising models. In Fig. 4, MC results are illustrated for some values of the model parameters taken from Fig. 3. Full red circles are critical points while full black ones are associated to T_{comp}. A qualitative agreement with Fig. 3 is achieved. $Tcomp$'s and T_c's are lower than in the MF case except in panel c where they are of the same order of magnitude.

Our calculations show some surprising results, the existence of first-order transitions for $h = 0$ and $D = 0$ in the present half-integer mixed-spin Ising model, in addition to the critical temperature T_c. It has been observed for very small and positive values of J_{cs}. Indeed, for $J_{cs} = 0.01$, $J_c = J_s = 1$, this happens at $T = 4.5$ whereas $T_c = 7.6$. The magnetization jump occurs from the (−3/2,5/2) phase

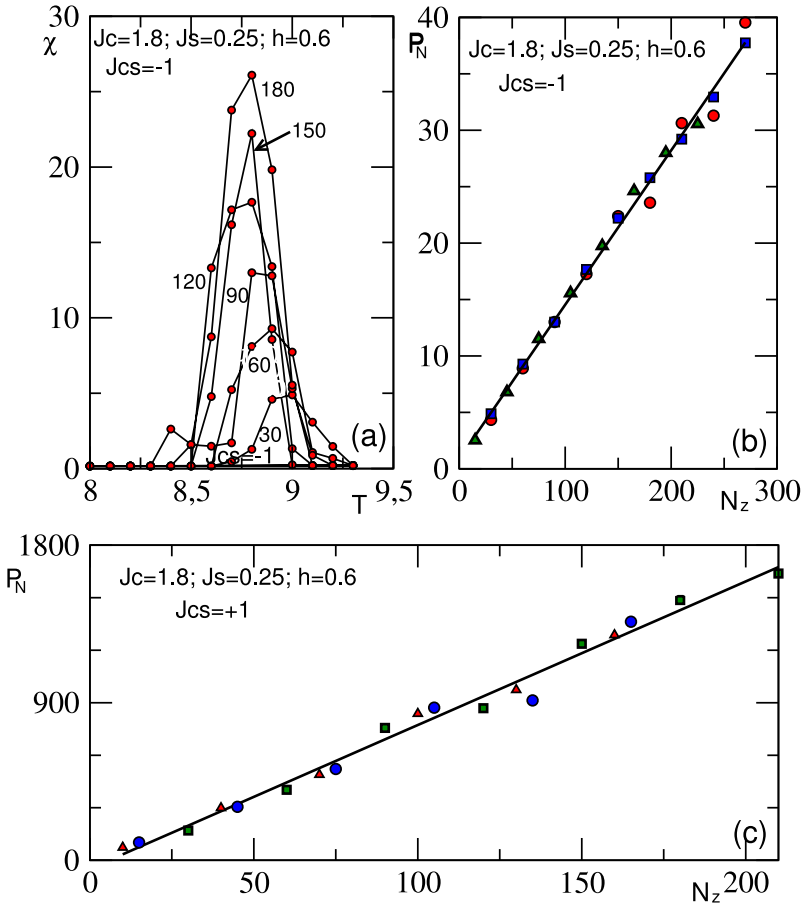

Fig. 7. Finite-size scaling analysis of the (first) peak height of χ observed in Fig. 6 as a function of the temperature T for selected Hamiltonian parameters written in the panels. In panel (a), curves of χ are plotted for six values of N_z written on the curves. In panels b and c, results of three different runs for the peak height of χ are shown for several values of N_z ranging from 10 to 270. Reported data are fitted to straight lines (solid lines). This linear scaling is a strong signature of the first-order nature of transitions indicated by these peaks observed in Fig. 6. The peak heights are very high in the case of the metastable-stable transition ($J_{cs} = +1$, panel c).

to the (+3/2,+5/2) phase. This first-order phase transition may be associated to a metastable-stable phase transition in the model. Such an existence has been also reported at low temperature in Ref. [47] on the mixed-spin (5/2,7/2) model investigated by means of the MF approximation.

4.2. Effects of an applied magnetic field

A magnetic field energy h is now applied over the system. Thermal energy will promote fluctuations of magnetic moments (spins) while h will try to align them. Such competitions among model parameters make the system's dynamics interesting and this section will essentially be concerned by MC results. Indeed, system properties change and first-order phase transitions appeared. It is well-known that such a transition may be accompanied by jump-like changes in the order parameters and hysteresis phenomena typical for temperature-induced first-order phase transitions [39,48,49]. Our simulations always started from the initial configuration (−3/2,+5/2). In Figs. 5a, c and 6a, c, an antiferromagnetic (AFM) value of J_{cs} is considered. Behaviors of M_c and M_s are displayed in Fig. 5a for $h = 0.6$ and for values of model parameters selected from Fig. 2a. This should help to show the effect of the applied magnetic field. It follows that M_s and M_c show jump-like discontinuities at the same temperature T. There, a temperature-induced magnetization reversal event occurs in core and shell materials. In Fig. 5c, the global magnetization M is depicted for $h = 0.6$ and $h = 0.4$. It emerges that jumps are also present and associated temperatures are different.

First, let us check whether saturation values of sublattice magnetizations observed in Fig. 5a are correct by studying energetics of possible ground state configurations that agree with selected values of the Hamiltonian parameters. Since the nanotube is a stacking of N_z sections in the z-direction, one isolated section may be simply considered. It has 54, 36 and 30 core–core, shell–shell and core–shell spin bonds respectively. Using expression of the Hamiltonian, one gets $(-3/2, +5/2)$ as the ground-state configuration with the energy $-398.25J_0$. The just higher energy $(-376.65J_0)$ is affected to $(+3/2, -5/2)$. One can therefore expect as it happens in Fig. 5a, that with an increase of thermal fluctuations, the core and shell magnetizations reversal event should occur at a given temperature. Second, let us analyze the ferromagnetic coupling case ($J_{cs} = 1$) of Fig. 5b. Here, the ground state configuration is $(+3/2, +5/2)$ with $-430J_0$ as energy. The just higher energy $(-344.25J_0)$ is associated to $(-3/2, -5/2)$. One remarks that the saturation value of M is −2 with the phase (−3/2,−5/2) at low temperature. It results that, the system is trapped during the simulations in a metastable state in a wide range of temperature. With increasing thermal fluctuations, this metastable state moves through jumps to the most stable $(+3/2, +5/2)$ state. Starting simulations with $(+3/2, +5/2)$ as initial configuration as shown in Fig. 5b (dashed and full lines), no jump is observed in the magnetizations. Global magnetization curves obtained from initial configurations (−3/2,+5/2) and (+3/2,+5/2) coincide after the jumps as observed in Fig. 5d. We check that the metastable-stable transition only occurs in a small range of the magnetic field energy.

The nature of the observed instability in both cases can be derived by analyzing the magnetic susceptibility χ and the internal energy U. These quantities are illustrated in Fig. 6a, c for $h = 0.4$ and $h = 0.6$.

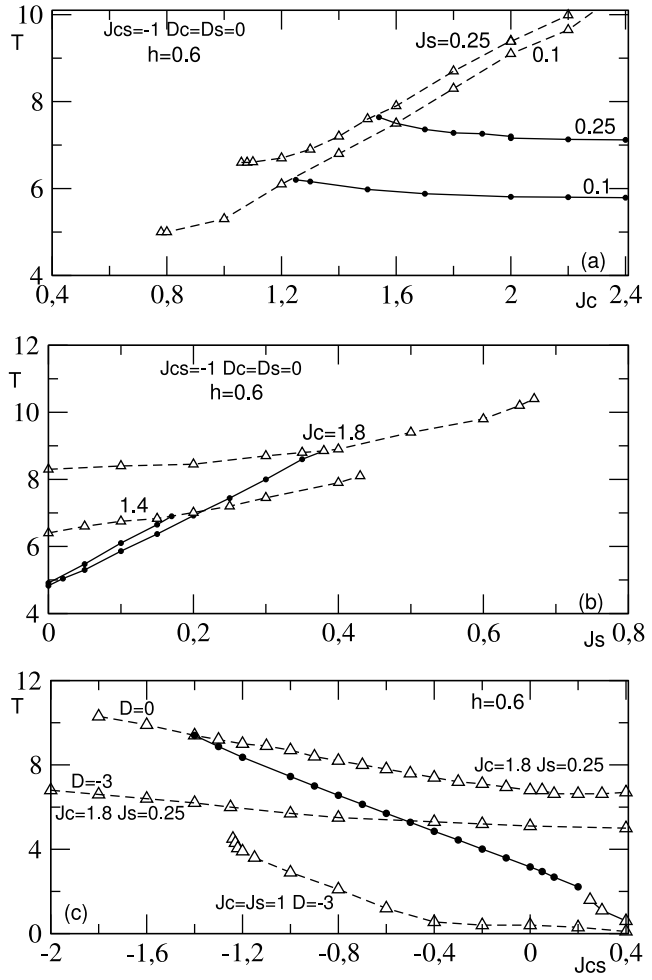

Fig. 8. Thermal phase diagrams for the nanotube in the (T, J_c), (T, J_s) and (T, J_{cs}) planes for selected values of model parameters. Lines with full circles and those with triangles are respectively associated to compensation temperature T_{comp} and first-order transition temperature T_{fo}. In different panels, most first-order transition lines terminate at end-points. This also happens for compensation lines.

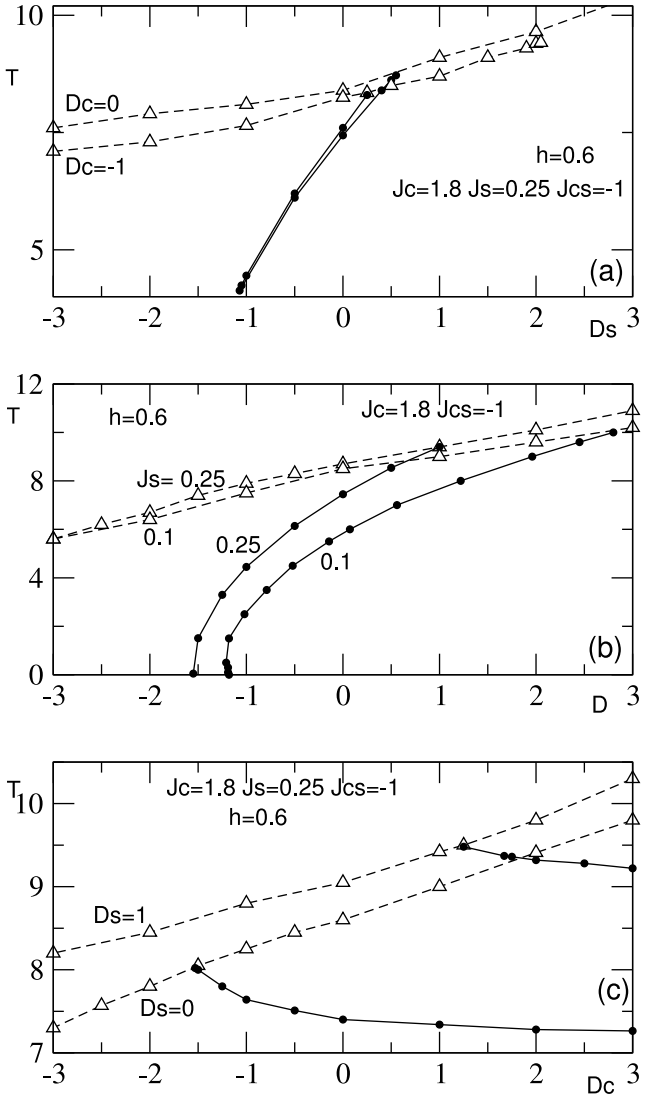

Fig. 9. Temperature phase diagrams in the (T, D_s), (T, D_c), $(T, Dc = Ds = D)$ planes for some selected values of model parameters written in the panels. Lines with full circles and those with triangles are respectively associated to compensation temperature T_{comp} and first-order transition temperature T_{fo}. At fixed values of D_s, T_{fo} increases with increasing values of D_c. Similar trends are observed at fixed values of D_c and increasing values of D_s. For the T_{comp}, the contrary is observed in panel (c) while in panel (a), it follows the same trend as T_{fo} when it exists.

For each value of h, two maxima are evidently observed on the χ-curves. The first one being very sharp and the associated temperature corresponds to discontinuities observed in Fig. 5c. A jump is also found in the trend of the internal energy U related to the free energy F by: $F = U - TS$. S denoting the system entropy. An anomalous behavior in U will effect F. Thus, following previous works [39,48,49] in the field, discontinuities observed in Figs. 5a, c and 6c at temperatures indicated by arrow (1) (h = 0.6) and arrow (2) (h = 0.4) in Fig. 6c, could be associated to first-order phase transitions. This also holds for the ferromagnetic (FM) interfacial coupling case with metastable state illustrated in Figs. 5b, d and 6.d for $h = 0.6$ where jumps are observed in M_c, M_s and U.

We performed a finite-size scaling analysis of the first peak height P_N of the magnetic susceptibility χ, where $N = N_t$ is the total number of spins in the system. For first-order phase transitions, P_N should scale linearly with N (see textbook Ref. [50]). By varying the number N_z of sections of the system given by $N = 36 \times N_z$, our calculations yield results illustrated in Fig. 7. Data plotted in Fig. 7b, result from three different MC simulations with statistical average over 10 independent runs each. The linear scaling $p_N \sim N$ appears evident and shows, without any doubt, the first-order nature of the macroscopic instability which occurred in the system in the negative interfacial coupling case. The case $J_{cs} = +1$ (Fig. 5b, d) is also investigated. A linear scaling form is also found as depicted in Fig. 7c. In the following, the first-order phase transition temperature will be denoted by T_{fo}. It is worthwhile to point out that these phase transitions prevail in a well-determined range of h's. T_{fo} is shifted to lower temperatures when h increases (Fig. 5c). From Fig. 5c, d, one notices that the ferromagnetic ordering region is amplified when the field energy increases. In Fig. 5c, the existence of the compensation temperature T_{comp} observed in Fig. 2a is preserved with the applied field and its value increases with the field energy. Through Figs. 5 and 6, it is also evidenced that the AFM coupling shows reacher properties than the FM case with the existence of the compensation point which is of high technological use (see below).

In Fig. 8, calculated steady state values of T_{comp} and T_{fo} are illustrated for varying values of coupling constants. Comparing Fig. 8a, b ($h = 0.6$) with Figs. 3, 4a, b ($h = 0.0$), one observes some similarities: same orientations and a tendency to coincide of T_{fo}-lines and T_{comp}-lines for increasing values of J_c and J_s. Moreover, T_{comp}-lines end on

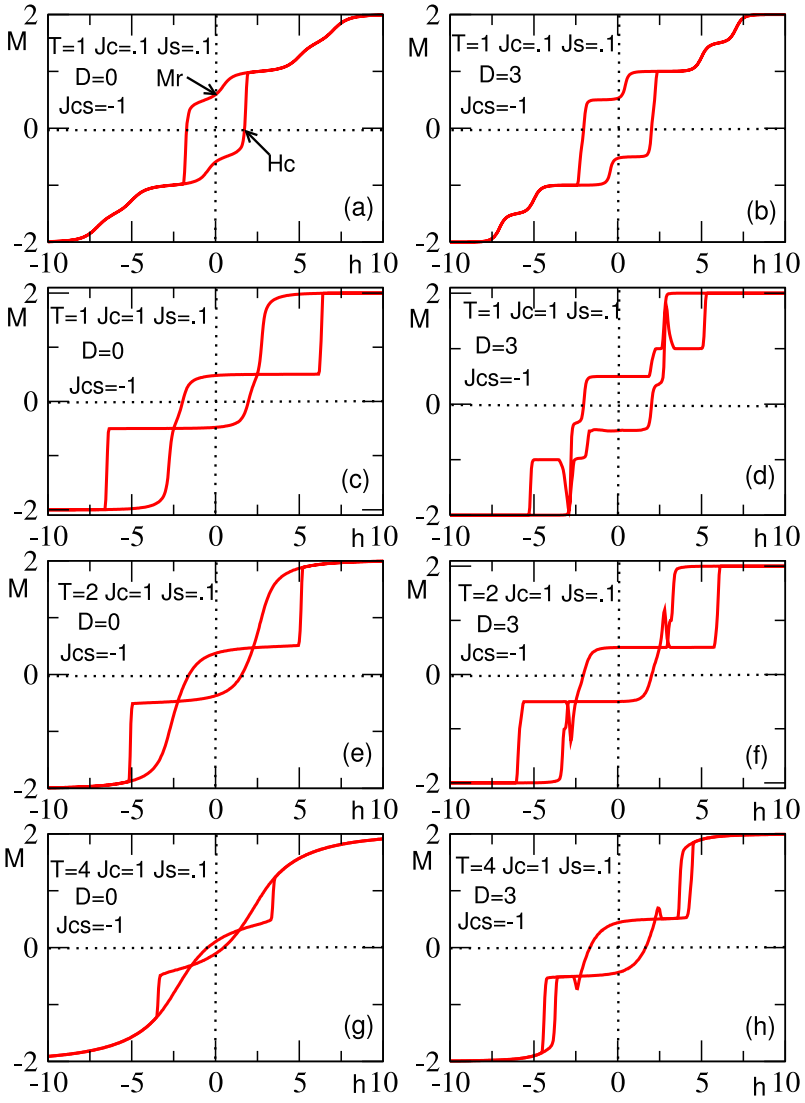

Fig. 10. Hysteresis cycles of the nanotube for core–shell coupling constant $J_{cs} = -1$ and various values of model parameters written in different panels. It could be observed the stabilizing effect of the crystal-field strength $D_c = D_s = D$ and the disordering one of thermal fluctuations. A critical hysteresis (with no loop) is obtained at very high temperature (e.g., at $T = 10$). The remanent magnetization M_r is obtained for $h = 0$ while the coercive field H_c is the one needed to bring the system magnetization to zero along the hysteresis cycle (see panel a).

T_{fo}-lines. The main difference is the existence of end-points in the presence of an applied field energy for T_{fo}-lines. We got in Fig. 8a as end-point coordinates: $(1.06; 6.56)$ for $J_s = 0.25$ and $(0.78; 5.0)$ for $J_s = 0.1$. The end-point travels to higher T's and J_c's for increasing J_s's. The same tendency is observed in panel (b). Just beyond termination points of T_{fo}-lines, the calculated global magnetization shows kink sites with no peak in the magnetic susceptibility χ.

The effect of J_{cs} on different transitions is depicted in Fig. 8c for selected values of J_c, J_s and h for $D = D_c = D_s = 0$ and $D = -3.0$. First, the negative crystal-field D is seen to lower T_{fo} and for this value of D, no T_{comp} has been detected. Second, for $D = 0$, the T_{comp}-line connects to two T_{fo}-lines. The low-temperature T_{fo} observed may be associated to a metastable-stable transition. Starting from the low temperature region, T_{fo}-lines turn left and finally exhibit end-points. Coordinates of the latters for $J_c = J_s = 1$ (not shown in panels) are: $(T = 2.92, J_{cs} = -0.52)$ for $h = 0$, $D = 0$; $(T = 4.96, J_{cs} = -0.16)$ for $h = 0.6$, $D = 0$. For $D = 2$ and $h = 0.6$, the behavior of the T_{fo}-line looks similar to the previous ones and terminates at the end-point $(T = 6.35, J_{cs} = -0.16)$. For $D = -3.0$ and $h = 0.6$ (Fig. 8c), the T_{fo}-line extends to the left and prevails for more negative values of J_{cs}.

In Fig. 9, we displayed results on the effect of core and shell anisotropies on T_{fo} and T_{comp} for $h = 0.6$ and selected values of exchange coupling constants. One observes in Fig. 9a, c that transition lines orientations are exactly those observed for $h = 0$ (Figs. 3, 4(c, d)). An end-point for T_{fo} is observed in panel (a) for $D_c = -1$. In Fig. 9b, it is observed that T_{comp}-lines start from the $T = 0$-axis, turn right and end on T_{fo}-lines. The end-point shifts towards negative values of D with increasing J_s's. One sees that when the anisotropy D_c or D_s decreases, it results a decrease of T_{fo} and this holds for all panels. Panel (b) shows that for suitable negative values of $D_c = D_s = D$ and other parameters, the compensation points lay very close to the zero-temperature axis.

Through out Figs. 8 and 9, one sees that the system subjected to an external magnetic field exhibits compensation points for suitable values of model parameters. This is an important issue. Indeed, an efficient optical control of magnetism in some physical compounds, needs the knowledge of proper conditions to achieve demagnetization or better

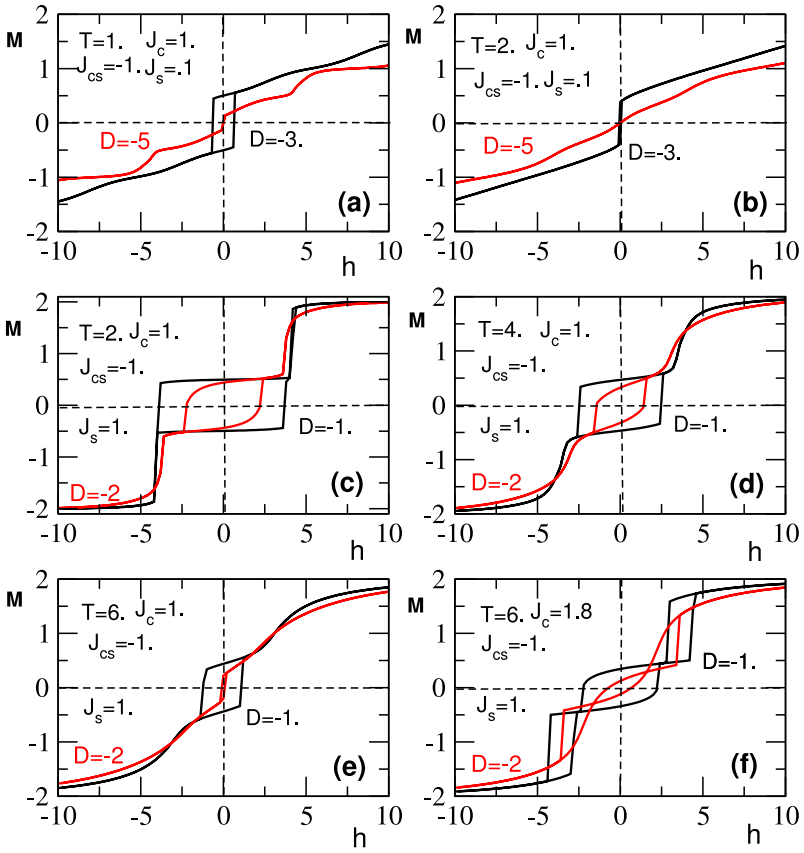

Fig. 11. Magnetic hysteresis cycles obtained for negative anisotropies and selected values of other model parameters.

subsystems magnetizations reversal that occurs at the compensation point [51,52].

4.3. Magnetic field hysteresis behavior

In Fig. 10, the hysteretic behavior of the system is illustrated for some selected values of the model parameters. It is observed that depending on the latters, one or multiple hysteresis cycles appeared. For small values of the coupling constants J_c and J_s with respect to J_{cs}, one central cycle is got (panel a). A non-zero applied value of D does not change the number of cycles but stabilizes phases that appear along the hysteresis cycles since some horizontal magnetization steps appeared (panel b). An increase of J_c increases the number of cycles to three (panel c). When a non-zero value of D is applied, an attempt to increase the cycles number is observed (panel d). The increase of thermal fluctuations brings some drawbacks since the surface of the cycles decreases (panels e and g). An applied crystal-field shows two effects: the appearance of other cycles (five in Fig. 10f, h) and the compensation of their surfaces which shrink by thermal fluctuations. An increase of the temperature decreases both the coercive field H_c and the remanent magnetization M_r of the system. The contrary holds with an increase of the crystal-field value D. The determination of coercivity and remanent magnetization is crucial for possible technological applications of the system. It emerges that the system showed interesting hysteresis behaviors such as multiple hysteresis cycles and may have many technological applications, in particular, in multi-state memory devices. The number of cycles can be modified by acting on some model parameters. It cannot however exceed the number of possible stable phases of the system when the parameter h varies. Critical hysteresis cycles are obtained in the high temperature range. In Fig. 11, we illustrated results for negative values of the anisotropy D. We found that when the absolute value of D increases, the area of the hysteresis loop shrinks. Therefore critical hysteresis is expected for large negative value of D. An analysis of results from different panels indicates that an increase of thermal fluctuations has the same effects on the hysteresis phenomenon as derived from Fig. 10.

5. Conclusion

In this work, an Ising nanotube with core spins 3/2 surrounded by shell spins 5/2 is investigated by means of Mean-Field calculations and Monte Carlo simulations with both positive and negative interfacial coupling constants. The effects of exchange interaction and crystal-field parameters on the nanotube magnetic properties have been examined in detail. Results by both methods on the order parameters and phase diagrams are compared in the absence of magnetic field energy and an impressive qualitative agreement was found. Beyond that, the model has been exclusively studied in the presence of a magnetic field by means of Monte Carlo simulations using the Metropolis sequential update algorithm. Stable and metastable system configurations are generated. Several typical phase diagrams are devised. It was shown that compensation, first-order transitions are got for suitable values of shell, core and core–shell coupling constants. For increasing values of the interfacial coupling constant J_{cs} at fixed other parameters, the transition temperature decreases. Richer phase diagrams are got for varying core and core–shell coupling and anisotropy constants. All these findings revealed the richness of the present model and should open new insights into magnetism of multicomponent nanotubes and nanowires and stimulate much experimental realizations.

CRediT authorship contribution statement

M. Karimou: Model conception, Numerical calculations, Manuscript writing, Revision processes. **T.D. Oke:** Model conception, Numerical calculations, Manuscript writing, Revision processes. **S.I.V.**

Hontinfinde: Model conception, Numerical calculations, Manuscript writing, Revision processes. **J. Kple:** Model conception, Numerical calculations, Manuscript writing, Revision processes. **F. Hontinfinde:** Model conception, Numerical calculations, Manuscript writing, Revision processes.

Declaration of competing interest

There are no conflicts to declare.

Data availability

No data was used for the research described in the article.

References

[1] R. Skomski, J. Phys.: Condens. Matter 15 (2003) R841.
[2] X. Zou, G. Xiao, Phys. Rev. B 77 (2008) 054417.
[3] Q.A. Pankhurst, J. Connolly, S.K. Jones, J. Dobson, J. Phys. D: Appl. Phys. 36 (2003) R167.
[4] S.J. Son, J. Reichet, B. He, M. Schuchman, S.B. Lee, J. Am. Chem. Soc. 127 (2005) 7316.
[5] D. Lee, R.E. Cohen, M.F. Rubner, Langmuir 23 (2007) 123.
[6] J. Kim, S. Park, J.E. Lee, S.M. Jin, J.H. Lee, I.S. Lee, I. Yang, J.S. Kim, S.K. Kim, M.H. Cho, T. Hyeon, Angew. Chem., Int. Ed. 45 (2006) 7754.
[7] A. López-Ortega, M. Estrader, G. Salazar-Alvarez, A.G. Roca, J. Nogués, Phys. Rep. 553 (2015) 1.
[8] R.H. Kodama, A.E. Berkowitz, E.J. McNiff, S. Foner Jr., Phys. Rev. Lett. 77 (1996) 394.
[9] T. Hayashi, S. Hirono, M. Tomita, S. Umemura, Nature 381 (1996) 772.
[10] J.E. Wegrowe, D. Kelly, Y. Jaccard, Ph. Guittienne, J.Ph. Ansermet, Europhys. Lett. 45 (1999) 626.
[11] A. Fert, L. Piraux, J. Magn. Magn. Mater. 200 (1999) 338.
[12] N. Saifuddin, A.Z. Raziah, A.R. Junizah, J. Chem. 2013, 676815, http://dx.doi.org/10.1155/2013/676815.
[13] S. Xie, W. Li, Z. Pan, B. Chang, S. Lianfeng, J. Phys. Chem. Solids 61 (2000) 1153.
[14] P.D. McGary, L. Tan, J. Zou, B.J.H. Stadler, P.R. Downey, A.B. Flatau, J. Appl. Phys. 99 (2006) 08B310.
[15] X.Y. Kong, Y. Ding, Z.L. Wang, J. Phys. Chem. B 108 (2004) 570.
[16] Y.C. Su, R. Skomski, K.D. Sorge, D.J. Sellmyer, Appl. Phys. Lett. 84 (2004) 1525.
[17] K. Lipert, M. Ritschel, A. Leonhardt, Y. Krupskaya, B. Büchner, R. Klingeler, J. Phys. Conf. Ser. 200 (2010) 072061.
[18] T. Kaneyoshi, Phys. Status Solidi b 248 (2011) 250.
[19] N. Hachem, I.A. Badrour, A. El Antari, A. Lafhal, M. Madani, M. ElBouziani, Chinese J. Phys. 71 (2021) 12.
[20] O. Canko, A. Erdinc, F. Taskın, A.F. Yıldırım, J. Magn. Magn. Mater. 324 (2012) 508.
[21] W. Wang, Y. Liu, Z.-Y. Gao, X.-R. Zhao, Y. Yang, S. Yang, Physica E 101 (2018) 110.
[22] E. Konstantinova, J. Magn. Magn. Mater. 320 (2008) 2721.
[23] M. Astaraki, M. Ghaemi, K. Afzali, Phys. Lett. A 382 (2018) 1291.
[24] R. Masrour, A. Jabar, Europhys. Lett. 128 (2019) 46002.
[25] J. Escrig, P. Landeros, D. Altbir, E.E. Vogel, P. Vargas, J. Magn. Magn. Mater. 308 (2007) 233.
[26] B. Lv, Y. Xu, D. Wu, Y. Sun, Particuology 6 (2008) 334.
[27] E. Konstantinova, J. Magn. Magn. Mater. 320 (2008) 2721.
[28] M. Masrour, L. Bahmat, M. Hamedoun, A. Benyoussef, E.K. Hlil, Solid State Commmunication 162 (2013) 53.
[29] L. Bahmad, R. Masrour, A. Benyoussef, J. Supercond. Nov. Magn. 25 (2012) 2015.
[30] R. Masrour, L. Bahmad, A. Benyoussef, J. Magn. Magn. Mater. 324 (2012) 3991.
[31] H.R. Liu, Q.F. Lu, X.F. Han, X.G. Liu, B.S. Xu, H.S. Jia, Appl. Surf. Sci. 258 (2012) 7401.
[32] J.H. Gao, Q.F. Zhan, W. He, D.L. Sun, Z.H. Cheng, Appl. Phys. Lett. 86 (2005) 232506.
[33] Y. Peng, T. Cullis, G. Mobus, X.J. Xu, B. Inkson, Nanotechnology 18 (2007) 485704.
[34] H.N. Hu, H.Y. Chen, S.Y. Yu, J. Magn. Magn. Mater. 299 (2006) 170.
[35] P. Schaaf, K. Zhang, C. Lange, A. Holz, M. Weisheit, S. Fähler, Appl. Surf. Sci. 253 (19) (2007) 8107.
[36] K.M. Takata, P.T.A. Sumodjo, Electrochem. Acta 52 (20) (2007) 6089.
[37] Yin-Zhong Wu, Dong-Lai Yao, Zhen-Ya Li, J. Appl. Phys. 91 (2002) 1482.
[38] S.N. Yaliraki, M. Kemp, Mark A. Ratner, J. Am. Chem. Soc. 121 (1999) 3428.
[39] N.F. Zounmenou, S.I.V. Hontinfinde, J. Kple, M. Karimou, F. Hontinfinde, Appl. Phys. A 126 (2020) 683.
[40] N. Maaouni, M. Qajjour, Z. Fadil, A. Mhirech, B. Kabouchi, L. Bahmad, W. Ousi Benomar, Physica B 566 (2019) 63.
[41] N.C. Metropolis, A.W. Rosenbluth, M.N. Rosenbluth, A.H. Teller, E. Teller, J. Chem. Phys. 21 (1953) 1087.
[42] Y. Shi-Lei, Z. Hai-Xia, Chin. J. Phys 15 (2006) 3026.
[43] T.D. Oke, F. Hontinfinde, K. Boukheddaden, Eur. Phys. J. B 86 (2013) 271.
[44] N.N. Bogoliubov, J. Phys. URSS 11 (1947) 23.
[45] R.P. Feynmann, Phys. Rev. 97 (1955) 660.
[46] M. Karimou, R.A. Yessoufou, G.D. Ngantso, F. Hontinfinde, A. Benyoussef, J. Supercond. Nov. Magn. 32 (2019) 1769.
[47] M. Karimou, R.A. Yessoufou, G. Dimitri Ngantso, F. Hontinfinde, E. Albayrak, Condens. Matter Phys. 22 (2019) 33601.
[48] A. Quetz, I. Dubenko, T. Samanta, H. Vinson, S. Talapatra, N. Ali, S. Stadler, J. Appl. Phys. 113 (2013) 17B512.
[49] A. Feraoun, M. Kerouad, Appl. Phys. A 124 (2018) 735.
[50] H.T. Diep, Physique de la Mattiere Condensée, Dunod, Paris, ISBN: 2100068520, 2003, (see page 235).
[51] I. Radu, K. Vahaplar, C. Stamm, T. Kachel, N. Pontius, H.A. Dürr, T.A. Ostler, J. Barker, R.F.L. Evans, R.W. Chantrell, A. Tsukamoto, A. Itoh, A. Kirilyuk, Th. Rasing, A.V. Kimel, Nature 472 (2011) 205.
[52] C.D. Stanciu, A.V. Kimel, F. Hansteen, A. Tsukamoto, A. Itoh, A. Kirilyuk, Th. Rasing, Phys. Rev. B 73 (2006) 220402.